INTEGRATED MULTI-FREQUENCY POLARIMETRIC AND INTERFEROMETRIC SAR PROCESSING TECHNIQUES

Jakob . Van Zyl, Anhua Chu, Scott Hensley, Yunling Lou, Yunjin Kim, Soren N. Madsen

Jet Propulsion Laboratory
California Institute of Technology
4800 Oak Grove Drive
Pasadena, California 91109

email jacobv@blacks.jpl. nasa.gov
fax: (818) 393-5285
phone: (818) 354-1365

ABSTRACT

The algorithms and implementation of an integrated SAR processor designed to process multi-frequency SAR data from either polarimetric, interferometric or mixed mode (a combination of polarimetric and interferometric modes) SAR systems is described, The processor is designed to automatically produce co-registered multi-frequency images regardless of the data collection mode at different frequencies. If at least one frequency interferometric DEM is available, all images are resampled and terrain corrected using the DEM. Examples are provided and discussed.

Submitted to *IEEE Transactions on Aerospace and Electronic Systems*

I. INTRODUCTION

Research on the utility of Synthetic Aperture Radar (SAR) data in many diverse applications has seen great activity in the past decade. In particular, two powerful SAR techniques emerged during this time. Polarimetric SARS were first demonstrated during the 1980's and are described by van Zyl et *al.* [1] and Zebker *et al.* [2]. Since then polarimetric SAR data have been applied to most disciplines of Earth Science. A recent summary of these investigations can be found in [3]. The second powerful SAR technique that has emerged and has received much attention lately is SAR interferometry. While first published by Graham [4] in the 1970's, interest in this technique has steadily increased since the demonstration of SAR interferometry using digital processing [5]. For a summary of the different applications of SAR interferometry, please see [6].

The processing techniques applied to interferometric SAR data typically depends on how the interferometer is implemented. In *repeat-pass* interferometry the interferometric base line is formed by observing the scene at two different times from two (slightly) different vantage points. This technique has been applied with great success to data acquired with spaceborne SAR systems, going as far back as the SeaSAT SAR [7,8]. In this implementation of interferometry it is common to process the two individual images into single-look images using traditional SAR processing, including deskewing the images [9]. The single-look images are then co-registered and the interferograms are formed outside of the traditional SAR processor. In the case of single-pass interferometers so far only implemented in airborne systems [10], [11] the two SAR images are acquired at the same time using two antennas physically separated in space with either along-track or cross-track separation. Madsen *et al.* [12] describe a processor implementation where both interferometric channels are processed simultaneously and the entire process, from image formation all the way to digital elevation model generation, is contained in one program. The aim of this TOPSAR processor, however, was primarily to produce the radar derived digital elevation model. Therefore, the accompanying radar image, although produced, was not radiometrically calibrated. This, of course was an implementation decision and not a fundamental limitation of the processing approach; with relatively little extra work the images could be radiometrically calibrated.

To really derive the maximum information content from SAR data, it is desirable to combine polarimetric and interferometric techniques, preferably at multiple frequencies, as more information about the scattering surface can be derived [13]. The NASA/JPL AIRSAR/TOPSAR system [14] is capable of simultaneously acquiring interferometric (C-anal/or L-band) and polarimetric data (C-, L- and P-band). In this paper we describe a processing approach that is used to process data acquired in any of these modes. This approach is different from that described in Madsen *et al.* [12] for the TOPSAR processor in both the motion compensation approach, as well as in the sense that data are deskewed

before interferograms are formed. Using this approach, the same basic SAR processor is used to process data acquired in any of the modes supported by the AIRSAR/TOPSAR system. In addition, the radar images are all radiometrically calibrated.

A brief description of the AIRSAR/TOPSAR system is first provided to set the stage for the discussion of the actual integrated processor to follow. The new integrated processor is then discussed in detail, including the coordinate systems and the motion compensation approach. This is followed by a discussion of the post processing algorithms, including the location algorithm used in the formation of the digital elevation model, and the radiometric correction algorithm applied to the SAR images, Finally, the interferometric calibration is discussed, and the results of this processor are compared with those obtained with an updated version of the TOPSAR processor described in [12].

II. THE AIRSAR/TOPSAR SYSTEM

The NASA/JPL AIRSAR system is a three-frequency airborne SAR system that was developed to be a general test-bed for developing various advanced SAR techniques. The SAR system is flown on a NASA DC-8 passenger jet, modified for research applications, operated by NASA's Ames Research Center in Mountainview, California. The AIRSAR antennas are not gimballed; instead the dual-polarized microstrip antennas are mounted fixed to the body of the DC-8 aft of the left wing. The earliest mode implemented in the AIRSAR system (operational since 1988) was the three-frequency polarimetric mode, where fully polarimetric data are acquired simultaneously at C-band, L-band and P-band. This mode was used to provide prototype data for the SIR-C /X-SAR science team [15] and many of the algorithms implemented for SIR-C data calibration and analysis were developed using AIRSAR data. At the same time, the addition of L-band and C-band antennas in front of the left wing, separated from the aft antennas by 20 m, made it possible to acquire along-track interferometric (ATI) data-at L-band C-band, while simultaneously acquiring polarimetric data at P-band [15,16]. Unfortunately, the 20 m baseline is too long at C-band for most practical ocean coherence times, resulting in C-band ATI data of questionable quality,

In 1990 NASA, in collaboration with an Italian consortium (CORISTA), approved the addition of another set of C-band antennas to implement a single-pass, fixed baseline cross-track interferometer (XTI) for topographic mapping. The C-band antennas were provided by CORISTA, while NASA sponsored the system modifications and processor development described by Madsen *et al.* [12]. This mode of the AIRSAR system became known as TOPSAR [1 O] and data have been acquired since 1991. The original TOPSAR processing software has been updated several times since the original publication in [12]. One version of this updated software was delivered to the Environmental Research Institute of Michigan (ERIM) under a contract with the Defence Advance Research

Projects Agency (DARPA), and is currently being used to process the data from the ERIM IFSARE system [24]. It should also be mentioned that the TOPSAR antennas were placed on the DC-8 in such a way that one of the TOPSAR antennas and the regular polarimetric C-band antenna could be used to form an along-track interferometer with a baseline of 1.2 m, resulting in vastly improved performance in the ATI mode.

In 1995 TOPSAR was extended to acquire XTI data simultaneously at C-band and L-band [18]. All TOPSAR interferometers can be operated in single or dual baseline modes. For single baseline operation signals are transmitted out of one antenna only, and the received signals are measured simultaneously through two antennas. In the dual baseline mode, signals are alternately transmitted out of the antennas at either end of the baseline, while the received signals are measured simultaneously through both antennas. The AIRSAR/TOPSAR modes are summarized in Table I.

III. PROCESSING APPROACH

The aim of the Integrated AIRSAR Processor is to implement a processing strategy capable of processing all the modes described above with the same basic processor. Therefore, the processor must automatically produce co-registered multi-frequency images, whether or not at least one frequency was acquired in the interferometric mode. Madsen *et al.* [12] describe a way to process single frequency cross-track interferometry data. In their approach, the individual images are never explicitly deskewed. Rather, the deskew is implicitly included in the location algorithm; the along-track offset given by Madsen *et al.* [12] is identical to the deskew used in the traditional range-Doppler processor [9].

This follows from the fact that in traditional (non-interferometric) SAR processing, it is assumed that the imaged pixel is located at the intersection of the Doppler cone (centered on the velocity vector), the range sphere (centered at the antenna) and an assumed reference plane, as shown in Figure 1. Since the Doppler cone has its apex at the center of the range sphere, and its axis of symmetry is aligned with the velocity vector, it follows that all points on the intersection of the Doppler cone and the range sphere lie in a plane orthogonal to the velocity vector. The additional information provided by cross-track interferometry is that the imaged point also has to lie on the cone described by a constant phase[1], which means that one no longer has to assume an arbitrary reference plane. This cone of equal phase has its axis of symmetry aligned with the interferometer baseline and also has its apex at the center of the range sphere. It then follows that the imaged point lies at the intersection of the Doppler cone, the range sphere and the equal phase cone, as shown in Figure 2. Using the same argument as before, it can be shown that the point

[1] Actually, the equi-phase surface is an hyperboloid, however, for most practical imaging geometries it may be considered to be a cone

still lies in a plane orthogonal to the velocity vector. This along-track offset can still be calculated using the traditional expression for the deskew, as shown in Madsen *et al.* [12].

When processing multi-frequency data, one has two options to ensure that the output images automatically co-register. In the first approach, the sub-patch size is chosen such that the same number of output lines are kept for all frequencies. (This assumes that the radars operate at the same pulse repetition frequency, which is the case for the AIRSAR system.) All frequencies can then be processed with properly scaled Doppler parameters, meaning that the along-track shift for all frequencies will be the same, regardless of the aircraft motion. Therefore, the location parameters derived at any frequency can directly be applied to all the other frequencies. In this case, the size of the sub-patch used, as well as the amount of overlap between adjacent sub-patches are determined by the length of the azimuth reference functions at the lowest frequency.

There are two main disadvantages to the approach described in the previous paragraph. First, the fixed number of output lines for all frequencies means that the processor becomes quite inefficient in the case of the high frequencies for which the azimuth reference functions are much shorter than at the low frequencies, since large parts of the overlap areas between successive sub-patches are unnecessarily recalculated. Secondly, since the size of the patch at the high frequencies is large compared to the synthetic aperture size, the motion compensation may be less than optimum.

These disadvantages can be overcome by processing each frequency separately into the zero squint geometry before utilizing any interferometric information. After the deskew is applied, the multi-frequency images automatically co-register. This now means that each frequency can be processed with a sub-patch size optimally chosen for that particular frequency. In a sense this follows the same processing paradigm usually employed in repeat-pass interferometry. The disadvantage, at least in our implementation, is that the bookkeeping of the phases during motion compensation is slightly more complicated.

IV. COORDINATE SYSTEMS AND MOTION COMPENSATION

The TOPSAR images are defined in a "global" sherical coordinate system denoted by (s,c,h), designed to locally approximate the earth's ellipsoid. Here s denotes the distance along the equator of the approximating sphere from a fixed point on the approximating sphere referred to as the *peg point*, c is the cross-track distance from the equator of the approximating sphere, and h is the height above the approximating sphere. We note further that the equator of the the approximating sphere coincides with the along-track direction in the SAR imaging geometry. Now let $\hat{\mathbf{s}}, \hat{\mathbf{c}},$ and h denote unit vectors in the s, c and h directions *at the platform location* as shown in Figure 3.

Since the TOPSAR antennas are not gimballed, we use another "local" coordinate system denoted by (x, y,z) to describe the instantaneous TOPSAR imaging geometry. To link the two coordinate systems, we note that

$$\mathbf{r}_{\hat{s}\hat{c}\hat{h}} = [\mathrm{Y}]\,[\mathbf{P}]\,[\mathbf{R}]\,\mathbf{r}_{xyz} \tag{1}$$

where the roll, pitch and yaw transformations are

$$[\mathbf{R}] = \begin{pmatrix} 1 & 0 & 0 \\ 0 & \cos r & -\sin r \\ 0 & \sin r & \cos r \end{pmatrix}; [\mathbf{P}] = \begin{pmatrix} \cos p & 0 & -\sin p \\ 0 & 1 & 0 \\ \sin p & 0 & \cos p \end{pmatrix}; [\mathbf{Y}] = \begin{pmatrix} \cos y & \sin y & 0 \\ -\sin y & \cos y & 0 \\ 0 & 0 & 1 \end{pmatrix} \tag{2}$$

respectively. A positive yaw turns the aircraft nose to the right of the flight path, a positive pitch raises the nose of the aircraft, and a positive roll lifts the left wing, Performing the matrix multiplication one finds that if $\hat{\mathbf{x}}$ is the unit vector pointing parallel to the aircraft fuselage taking into account aircraft yaw, pitch and roll,

$$\hat{\mathbf{x}} = \begin{pmatrix} \cos p \cos y \\ -\cos p \sin y \\ \sin p \end{pmatrix} \tag{3}$$

Since the TOPSAR antennas are mounted fixed to the body of the aircraft pointing to the left of the aircraft, the imaging plane is to the left of $\hat{\mathbf{x}}$, and perpendicular to it. To define this plane, we pick a horizontal vector $\hat{\mathbf{y}}$, perpendicular to $\hat{\mathbf{x}}$ and $\hat{\mathbf{h}}$, i.e.

$$\hat{\mathbf{y}} \cdot \hat{\mathbf{x}} = 0\,; \quad \hat{\mathbf{y}} \cdot \hat{\mathbf{h}} = 0 \tag{4}$$

from which it follows that

$$\hat{\mathbf{y}} = \begin{pmatrix} \sin y \\ \cos y \\ 0 \end{pmatrix} \tag{5}$$

The "local" coordinate system is completed by defining $\hat{\mathbf{z}}$ to be perpendicular to both $\hat{\mathbf{x}}$ and $\hat{\mathbf{y}}$, i.e. $\hat{\mathbf{z}} = \hat{\mathbf{x}} \times \hat{\mathbf{y}}$, from which it follows that

$$\hat{\mathbf{z}} = \begin{pmatrix} -\cos y \sin p \\ \sin y \sin p \\ \cos p \end{pmatrix} \tag{6}$$

Using this local coordinate system, we define the line-of-sight vector $\hat{\mathbf{n}}_{los}$ to point from the point being imaged to the radar as:

$$\hat{\mathbf{n}}_{los} = -\sin\theta\,\hat{\mathbf{y}} + \cos\theta\,\hat{\mathbf{z}} \tag{7}$$

Here θ is the look angle, which is still unknown. By combining the previous expressions we find that

$$\hat{\mathbf{n}}_{los} \cdot \hat{\mathbf{h}} = \cos e \cos p \tag{8}$$

But, from the imaging geometry,

$$\hat{\mathbf{n}}_{los} \cdot \hat{\mathbf{h}} = H/\rho \tag{9}$$

where H is the altitude of the aircraft above the point being imaged, and p is the slant range to the target in the squinted geometry *measured from the global reference track.* The reference tracks will be discussed in more detail below. The incidence angle is now easily calculated from (8) and (9) as

$$\cos\theta = \frac{H}{p\cos p}. \tag{lo}$$

The Integrated Processor is implemented using the well-known range-Doppler algorithm. The first step in the processing is range compression, as described in Curlander and MacDonough [9]. Before azimuth compression the range compressed signals must first be compensated for the deviation of the aircraft from an assumed straight line flight path. To do this, we first generate arrays with (x, y, z) coordinates of the actual tracks of both the transmit and receive antennas, based on the aircraft position and attitude information as measured by the radar inertial navigation unit (INU), and the leverarms describing the positions of the antennas relative to that of the INU. The effective antenna reference track is the mean location of the actual transmit and receive tracks. Let us call this effective antenna track $\mathbf{r}_a$ **(see** Figure 4): ‘

$$\mathbf{r}_a\ \mathbf{(kc)} = \left(x_a(line), y_a\ (line),\ z_a(line)\right), \tag{11}$$

where *line* denotes the raw data pulse number. The global reference track $\mathbf{r}_g$ is denoted by

$$\mathbf{r}_g\ \mathbf{(fine)} = (line \bullet \Delta x, y_g, z_g) \tag{12}$$

with Δx the along-track pixel spacing between two successive radar pulses. The variables y_g and z_g describe the average flight path (as measured by the INU) in the cross-track and

vertical directions, respectively. This fit is done using the entire data set to be processed, i.e. using all the motion data for the entire image to be processed.

The motion compensation is done in two steps. First, we calculate a local reference track for each patch, by calculating the least squares fit in the cross-track and vertical directions using only the motion data corresponding to the image data for the current patch. Let us denote this by **r,**

$$\mathbf{r}_l(line) = (line \bullet Ax,\ y_l, z_l) \tag{13}$$

Note that the parameters y, and z_l are calculated to be the least squares fit to the cross-track and vertical deviations of the aircraft from a straight line *parallel to the global reference track.* This choice reduces the amount of resampling to be done during the deskew process.

For each pulse, we now calculate the deviation of the aircraft from this local reference track:

$$\mathbf{d}(line) = \mathbf{r}_a(line) - \mathbf{r}_l(line) \tag{14}$$

Next, we calculate the line-of-sight vector for each range bin using (7) and an assumed reference height for the terrain imaged. The slant range offset to be compensated for is

$$\Delta\rho_{a\to l} = -\hat{\mathbf{n}}_{los} \bullet \mathbf{d}(line) = -\hat{\mathbf{n}}_{los} \bullet (\mathbf{r}_a - \mathbf{r}_l) \tag{15}$$

The phase correction that must be applied to compensate for the difference in two-way propagation paths is

$$\Delta\phi_{a\to l} = -\frac{4\pi}{\lambda}\Delta\rho_{a\to l} \tag{16}$$

In our implementation, the slant range offsets are calculated using 64 equally spaced points in both range and azimuth. Since this quantity varies slowly, it is not necessary to calculate this for each pixel in the image. To find the offset for each pixel, we interpolate this sparse array using a linear interpolation. The range compressed data are then interpolated using a sine interpolator to account for the range shift, and the phase shift corresponding to A $\rho_{a\to l}$ is applied to the interpolated data.

The next step in the processing is to perform azimuth compression. During azimuth compression, we also transform the geometry from the local squint angle assumed in processing the current patch to the zero squint (or deskewed) geometry. As mentioned before, without this step, the multifrequency images will not be co-registered. In addition, the geometry must also be transferred from the local to the global reference

track. Note that the phase of the signal still represents the phase at the local squinted geometry. The reason for this hybrid approach is that it simplifies the height reconstruction and geolocation algorithm to be discussed later.

The first step in azimuth compression is to transform the motion compensated range compressed data to the azimuth frequency domain. This is followed by range migration interpolation, To ensure accurate range migration correction even at P-band, we implemented the exact range migration equation [9] in the Integrated Processor. For improved efficiency we include the range resampling to transfer from the local reference line to the global reference line in the range migration calculation,

The azimuth reference function should take into account the fact that the range now is the slant range at zero Doppler. During azimuth compression, we also shift the signal by the fractional part of the azimuth deskew. This means that the deskew program only has to shift images by integer number of pixels. The fractiona deskew is accomplished by multiplying the frequency domain data by a phase ramp

$$D(f) = \exp\{-2\pi f \delta\} \tag{17}$$

where δ is the fractional part of the deskew, and f is the azimuth frequency relative to the along-track sampling frequency.

The final step in the processing is to account for the phase shift due to the change in the geometry from the local reference line to the global reference line, As before (see (16)), this phase shift is

$$\Delta\phi_{l\to g} = -\frac{4\pi}{\lambda}\Delta\rho_{l\to g} \tag{18}$$

with

$$\Delta\rho_{l\to g} = \hat{\mathbf{n}}_{los}\cdot\left(\mathbf{r}_l - \mathbf{r}_g\right) \tag{19}$$

This phase shift is applied after azimuth compression. Note that when $\hat{\mathbf{n}}_{los}$ is calculated for use in (19), the range in the squinted geometry is used, and $\hat{\mathbf{n}}_{los}$ points from the pixel to the *global* reference track. This ensures that the same definition is used for $\hat{\mathbf{n}}$,., throughout the processor, and simplifies the location algorithm to be used later on to position pixels in the final radar image.

Following azimuth compression, the data are deskewed by shifting each range bin by the integer part of the deskew. The final single-look image is now in the zero Doppler slant range geometry where mu] ti-f requency images automatically y co-register after residual

cable length differences in the radar system are taken into account. If no interferometric data are available, the data are multi-looked, radiometrically corrected for the range fall-off, and the antenna patterns and scattering area assuming a flat earth are removed. Polarimetric data are further combined and translated into the standard JPL compressed Stokes matrix format [23].

We note here that our implementation of motion compensation differs from that described by Madsen *et al.* [12] for the TOPSAR processor in two ways. First, all images are referenced to a common global reference line. This effectively means that the phase due to a flat earth is explicitly removed during the interferometric SAR processing. The resulting interferogram therefore only contains the phase difference due to the topographic variation from the assumed reference plane. Second, all local reference lines are parallel to the global reference line. While this is not the optimum solution in terms of removing the smallest amount of motion, it means that the imaging geometry after motion compensation is the same for all patches, and therefore, the patches can easily be combined into one long strip. This also ensures that multi-frequency and non-interferometric data will be co-registered, In the case of the TOPSAR processor described by Madsen *et al.* [12], motion compensation is performed to the best fit local reference line for each patch. In this way, the motion compensation is optimized for each patch. However, the imaging geometry after motion compensation may be different from patch to patch. Since in their case they only processed single frequency interferometric data, and each patch is seperately phase unwrapped and geometrically resampled, the final images also appear as one strip. As mentioned before, however, the TOPSAR approach cannot be used to process and automatically co-register multi-frequency data that involves non-interferometric modes, since the imaging geometries will be different for the different frequencies. To ease data analysis for the many Earth science applications that require multi-frequency and polarimetric SAR data, it is very important to automatically produce co-registered images.

V. LOCATION ALGORITHM

If interferometric data were acquired, the two interferometric channels are cross-correlated and averaged and the resulting phase is unwrapped using the algorithm first proposed by Goldstein, *et al.* [7]. Once the phases have been unwrapped, the exact geometry of the image can be reconstructed.

The image geometry is reconstructed in the (s,c,h) basis. If we know exactly where the target is in space, we can write an expression for its location as

$$\mathbf{T} = \mathbf{P} - \rho\hat{\mathbf{n}} \tag{20}$$

1.

where **T** represents the target location, **P** represents the aircraft location (known from the INU ro differential GPS measurements), *p* is the range to the target at the time of imaging, and $\hat{\mathbf{n}}$ is the unit vector that points from the actual target location to the radar. During processing this unit vector is approximated by $\hat{\mathbf{n}}_{los}$ assuming a flat earth. The interferometric phase provides us with a means to determine the actual unit vector $\hat{\mathbf{n}}$, and through (20) to determine the position of the target,

We start by assuming that the velocity vector points along the $\hat{\mathbf{s}}$ direction, *i.e.*

$$\mathbf{v} = v\hat{\mathbf{s}}. \tag{21}$$

The Doppler cone is given by

$$f_d = -\frac{2v}{\lambda}\hat{\mathbf{n}}_{los}\cdot\hat{\mathbf{s}} \qquad \Rightarrow \qquad n_s = -\frac{\lambda f_d}{2v} \tag{22}$$

As mentioned before, this along-track component of the line-of-sight vector is not affected by the value of the interferometric phase, since the position of the target lies in the intersection of the Doppler cone and the range sphere, i.e. in a plane perpendicular to $\hat{\mathbf{s}}$. The only remaining unknowns are now the c and *h* components of ii.

From the interferometric imaging geometry, it is easily shown [12,11] that if the range to the target is large compared to the length of the interferometric baseline, the phase difference measured by the interferometer can be written as

$$\phi = \frac{4\pi}{\lambda}\hat{\mathbf{n}}\cdot\mathbf{B} \tag{23}$$

where the factor 4π follows from the fact that the antenna position is defined to be the average of the transmit and receive antenna positions, and **B** is the physical interferometer baseline. Equation (23) describes the phase cone shown in Figure 2.

As described in the previous Section, in the Integrated Processor, motion compensation is performed to a common reference line. This means that four different phases are added to the two interferometric channels during processing: two each to move the reference from the actual antennas to the two (different) local reference lines, and two each to move the reference from the two local reference lines to the common global reference line, as shown by the arrows in Figure 4. When forming the interferogram after all images are referenced to a common global reference line, therefore, the resulting interferometric phase can be written as (see (23), (15) and (18))

$$\phi = \frac{4\pi}{\lambda}\left(\hat{\mathbf{n}}_{los} - \hat{\mathbf{n}}\right)\cdot\mathbf{B} \tag{24}$$

To solve for the remaining components of the line-of-sight vector, we rewrite these vectors as

$$\hat{\mathbf{n}}_{los} = n_s\hat{\mathbf{s}} - \cos\alpha_{ref}\sqrt{1-n_s^2}\,\hat{\mathbf{c}} + \sin\alpha_{ref}\sqrt{1-n_s^2}\,\hat{\mathbf{h}} \quad \textbf{(25)}$$

and

$$\hat{\mathbf{n}} = n_s\hat{\mathbf{s}} - \cos\alpha\sqrt{1-n_s^2}\,\hat{\mathbf{c}} - \sin\alpha\sqrt{1-n_s^2}\,\hat{\mathbf{h}} \quad \textbf{(26)}$$

Now, using (25) and (26) in (24) we find:

$$\phi = \sqrt{1-n_s^2}\;\frac{4\pi}{\lambda}\left[B_h\left(\sin\alpha_{ref} - \sin\alpha\right) - B_c\left(\cos\alpha_{ref} - \cos\alpha\right)\right] \quad (27)$$

or

$$B_c\cos\alpha - K = B_h\sin\alpha \quad \textbf{(28)}$$

wj th

$$K = \frac{\lambda\phi}{4\pi\sqrt{1-n_s^2}} - B_h\sin\alpha_{ref} + B_c\cos\alpha_{ref} \quad \textbf{(29)}$$

To solve for α from (28), we start by squaring both sides of (28) and then solve for cos α. The result is

$$\text{Cos}\,\alpha = \frac{1}{B_c^2 + B_h^2}\left\{B_cK + B_h\sqrt{B_c^2 + B_h^2 - K^2}\right\}, \quad (30)$$

where we resolved the sign of the square root, by insisting that for ϕ = O, we should have Cos α = Cos arc,.

Equations (30), (29), (26), (22) and (20) now completely define the actual location of the target. This solution, however, describes the position of the target in a Cartesian coordinate system that is locally tangent to the surface of the earth. A more convenient and useful representation of the target position is a spherical coordinate system where the target height is expressed as a height above some reference ellipsoid.

Let **T** be the position of the target in the Cartesian coordinate system, and **T'** be the position of the target in the spherical coordinate system, For a definition of the variables, see Figure 5. From the geometry shown in Figure 5 one can extract the right triangle shown in Figure 6 and obtain the following expression for *h'* in terms of *h.*

$$h' = (R_e + h)\sqrt{1 + \frac{(c_p - \rho n_c)^2 + (s_p - \rho n_s)^2}{(R_e + h)^2}} - R_e \tag{31}$$

where R_e is the distance from the center of the earth to the reference ellipsoid, *i.e.* the radius of the approximating sphere. An approximate form of the expression (31), valid for airborne imaging geometries, is obtained by using the first two terms in a Taylor series expansion of the square root:

$$h' = h_p - \rho n_h + \frac{(c_p - \rho n_c)^2 + (s_p - \rho n_s)^2}{2(R_e + h_p - \rho n_h)} \tag{32}$$

To find the corrections to the along-track and cross-track positions of the target, we apply Napier's rules for right spherical triangles to the spherical triangle shown in Figure 5. This yields the following expressions:

$$s' = R_e \tan^{-1}(\tan\mu \cos\gamma); \quad c' = R_e \sin^{-1}(\sin\mu \sin\gamma) \tag{33}$$

where., from Figure 5,

$$\tan\mu = \frac{(c_p - \rho n_c)^2 + (s_p - \rho n_s)^2}{R_e + h_p - \rho n_h} \tag{34}$$

and

$$\sin\mu = \sqrt{\frac{(c_p - \rho n_c)^2 + (s_p - \rho n_s)^2}{(c_p - \rho n_c)^2 + (s_p - \rho n_s)^2 + (R_e + h, - \rho n_h)^2}} \tag{35}$$

From Figure 5, it is seen that

$$\cos\gamma = \frac{s}{\sqrt{(c_p - \rho n_c)^2 + (s_p - \rho n_s)^2}} \tag{36}$$

and

$$\sin\gamma = \frac{c}{\sqrt{(c_p - \rho n_c)^2 + (s_p - \rho n_s)^2}} \tag{37}$$

Retaining the first two terms in the Taylor series expansion of sin-' x in (33), and simplifying the resulting expression using (35) and (37), and Taylor series expansions for the square roots, and keeping in mind that in general $s << R_e + h - \rho n_h$, one can show that

$$c' = c_p - \frac{R_e}{R_e i\text{-} h_p - \rho n_h} \rho n_c . \tag{38}$$

A similar derivation using the approximation that tan-l x ≈ x for small x shows that

$$s' = s_p - \frac{R_e}{R_e + h_p - \rho n_h} \rho n_s . \tag{39}$$

The Integrated Processor uses a local spherical approximation to the WGS-84 ellipsoid [25] as the reference ellipsoid. A more complete discussion of the coordinate system-s used, and the derivations of the location algorithm will be provided in a future paper by Hensley and Madsen [26].

VI. RADIOMETRIC CORRECTION

The radiometric correction of polarimetric SAR Images is now well understood, and we will only mention the major elements of our implementation here. The first step is to perform the phase calibration. We use the algorithm previously described by Lou and van Zyl [19] utilizing calibration tones to automatically calibrate the phases without the use of external calibration devices. Actually, a calibration image with calibration devices is used to derive a single phase constant for each frequency. This is done only once for each radar flight season unless the physical radar configuration is changed. After this single constant has been derived, phase calibration for subsequent images is automatic.

The second step is to remove the antenna cross-talk as described by van Zyl [20]. Third, the different polarization channels are balanced using calibration constants derived from a calibration image. These amplitude calibration constants, like the phase constants, are derived only once per flight season using the power integration method described by Gray *et al.* [21].

The method used to remove the scattering area and the antenna gains depends on whether interferometric data were acquired or not. If interferometric data were not acquired, the radiometric corrections are performed assuming a flat earth, as is customary in traditional airborne SAR processing. When interferometric data are available, the approach described by van Zyl et *al,* **[22]** is used to remove the scattering area and antenna gains. This approach uses the digital elevation model derived from the interferometric data to calculate the actual scattering area and the actual look angle for each pixel. This

actual look angle is then used to calculate the antenna gain that must be removed during the radiometric calibration. Here, we only summarize the calibration procedure. For more information, see *[22].*

From the radar equation, it follows that the received power from a scattering element of area *A* is given by

$$P_r = \frac{P_t G_t(\theta) G_r(\theta) \sigma^0 A \lambda^2}{(4\pi)^3 \rho^4} \qquad (40)$$

where P_t is the transmitted power, $G_t(0)$ and $G_r(0)$ are the transmit and receive antenna gains, respectively, and σ^0 is the normalized radar cross-section for the area *A*. Note that *A* is the area *on the ground* responsible for the scattering, As before, λ is the radar wavelength and *p* is the slant range to the pixel.

During traditional airborne SAR processing, a flat earth is usually assumed for purposes of calculating the radar look angle and scattering element sizes. It is assumed that the radar platform was at an altitude *H* above a flat earth reference plane. Under this flat earth assumption, the look angle and the local incidence angle for a given pixel are the same. Since the radar signals are sampled in the time domain, which corresponds to distances in the line-of-sight (the slant range) direction, the following approximation is usually made during SAR processing when calculating the scattering element size:

$$A = \frac{\delta_r \delta_a}{\sin\theta} \qquad (41)$$

where δ_r and δ_a are the slant range (cross-track) and azimuth (along-track) pixel spacings, respectively. Note that the area is defined by the pixel spacings, not the resolutions. The goal of SAR imaging is to measure σ^0 for each pixel. Rewriting (40), one finds that

$$\sigma^0 = K(\rho, 0)/A \qquad (42)$$

where

$$K(\rho, e) = \frac{(4\pi)^3 \rho^4}{G_t(\theta) G_r(\theta) \lambda^2} \frac{P_r}{P_t} \qquad (43)$$

We note that, apart from the measured transmit and received power levels, two parameters, *p* and θ, must be estimated to remove $K(\rho, \theta)$. The slant range *p* to the scattering area is measured directly by the radar, and is therefore known very accurately. The look angle θ, however, is only measured directly if interferometric data are acquired,

and must be inferred indirectly for all other AIRSAR/TOPSAR modes. In most non-interferometric SAR processors, this angle is calculated using the altitude of the radar platform, H , above the reference plane, the slant range p, and assuming a flat earth. If this assumption is correct, one can write

$$\cos\theta = H/p \tag{44}$$

Finally, to complete the calibration, one has to remove the scattering element size A. Again most SAR processors use the flat earth assumption and approximate the area A by (41). In the Integrated Processor, the non-interferometric modes are calibrated using (41)-(44).

When interferometric data are available, one can directly estimate the look angle θ from the interferometric phase. Also, since a digital elevation map is derived from the interferometric phase, one can use this digital elevation information to estimate the size of the scattering element directly. As shown in [22], if the projected area of surface element tilted in an arbitrary direction is $\delta_r \delta_a$, the actual area is

$$A = \frac{\delta_r \quad \delta_a}{\sin(\theta - \alpha_r)\cos(\alpha_a)} \tag{45}$$

where α_r is the tilt of the surface in the range direction (positive values mean tilts towards the radar) and α_a is the tilt of the surface in the azimuth direction (positive values mean tilts in the direction in which radar platform is moving). The look angle θ must be estimated from a knowledge of the slant range p, the radar-platform altitude H and the elevation of the pixel above the reference plane, h, and can be calculated as

$$\cos\theta = (H - h)/\rho \tag{46}$$

The Integrated Processor uses (45) and (46) in (42) and (43) to calibrate the SAR images in the TOPSAR mode.

As an illustration, consider the image of Tennesey Valley near San Francisco in California shown in Figure 8. This dataset was acquired in the TOPSAR mode, with the C-band radar operating in the interferometric mode, and the L-band and P-band radars operating in the polarimetric mode. The images shown are the C-band VV data. The data set covers part of Marin County just north of San Francisco, with the Golden Gate bridge visible in the bottom of the images. The image on the left was calibrated using the interferometric information, and equations (45) and (46) above, while the image on the right was calibrated using the flat earth approximation, *i.e.* equations (41) and (44). The image on the right shows much larger difference in radar cross section between slopes facing the radar and those facing away from it. This almost creates the illusion of a three-dimensional effect in the image on the right. Comparing the two images, it is clear that

most of the brightness modulation in the image on the right is no longer present in the image on the left. This means that most of the difference in brightness between the slopes facing the radar and those facing away from it is in fact due to the uncompensated scattering areas, and not really due to the influence of the incidence angle on the scattering from the terrain. This general trend of a reduction in the modulation is observed in all images produced when topography is taken into account during calibration, although the exact amount of reduction is of course a function of the scattering law of the type of terrain.

We note here that removing the effects of topography during radiometric calibration can have a significant effect on the polarization response of a pixel, as discussed in van Zyl *et al. [22]*. This follows from a closer examination of equation (43). Since the antenna gains are typically different for the different polarizations, the effect of the topography on (43) will also be different for the different polarizations. Since many geophysical algoritms depend on calculating ratios of radar cross sections measured at different polarization combinations, this correction could significantly improve the accuracy of some geophysical algorithms.

VII. INTERFEROMETRIC CALIBRATION

The height errors in an interferometric radar DEM (Digital Elevation Map) can be classified into two types: relative and absolute errors. Relative errors result from the pixel-to-pixel uncorrelated phase noise which cannot be compensated by a calibration technique. Absolute errors are systematic in nature and may be caused by various error sources such as the differential phase due to receiver and transmitter channel imbalance and baseline estimation errors. Unlike relative errors, absolute errors can be compensated by using ground control points if these errors are stable in time. This compensation process is an essential part of the interferometric calibration procedure. Detailed formulations and techniques of the interferometric calibration procedure are given elsewhere [27],

The interferometric calibration procedure starts with co-registration of two images. We accomplish this co-registration by applying a complex (both amplitude and phase) correlation technique to two single look complex SAR images. After this co-registration process, the two images are usually co-registered to an accuracy much better than 1/100 of a pixel. The second step is to remove a slant range bias. This is done by measuring the round-trip time from the SAR to surveyed targets whose locations are known accurately. (The slant range bias is caused by incorrectly estimated radar electronic delay time since a radar measures the elapsed time including both electronic delay inside the radar and true round trip time,) We have used corner reflectors at the Rosamond lakebed in southern California to perform this slant range calibration. In this process, tropospheric refractive

index variations must be considered since the round trip time is determined by the optical path length rather than the physical length.

In order to accurately reconstruct the digital elevation model from the interferometric phase, the locations of the two interferometric antennas must be known accurately, For the NASA /JPL TOPSAR case, the baseline length and attitude must be known to an accuracy better than 1 mm and 0.01 degrees, respectively to achieve a height accuracy of *2* m. The separation of the interferometric antennas are surveyed accurately before SAR data collections. In addition, their absolute locations during the flight can be calculated using the motion data obtained from the Honeywell IGI (Integrated GPS/INU) system. The baseline vector estimation bias can be calibrated out using surveyed corner reflectors. The aircraft attitude measurement bias can also be estimated by comparing the Doppler centroid derived from the aircraft motion data and one from radar phase history data. For the TOPSAR case, the bias has been measured to be almost negligible. Using the Honeywell IGI, we measured the aircraft velocity and timing accurately. The radar frequency must be calibrated by comparing the STALO frequency with the frequency standard. Since the final RF frequency, after frequency up-conversion, can also be measured accurately (~ 10-8), no significant calibration effort is needed.

The next step is to evaluate the receiver channel imbalance, especially in phase, The phase difference can be measured by injecting the same calibration tone signal into both receiver channels. However, any imperfections associated with the calibration tone measurement would cause a differential phase estimation error, This error also can be removed by comparing a radar DEM with surveyed corner reflectors.

The errors discussed in the previous paragraphs cause similar height error signature in DEM. Therefore, it is rather difficult to identify each error source from the DEM height errors since they are likely caused by a combination of various error sources. This process becomes even more difficult if the height error data have been obtained without sufficient incidence angle variation.

There may also be additional error sources that have not been modeled in the calibration procedure, which would cause the error estimation to be biased.' As an example, multi-path reflections from various parts of the aircraft fuselage can cause such a bias. Furthermore, the phase error caused by the presence of the multipath signal usually changes as a function of the incidence angle. Since the multi-path sources are usually unknown and it is difficult to model this multiple scattering from a complex structure like an aircraft, one must apply a different approach to the calibration problem to remove the effect of these kinds of errors. This technique is known as a generalized *phase screen* and includes all errors simultaneously. This technique involves estimating a correction function (also known as a phase screen) over the angles of incidence to the aircraft. (In general, it is desirable to measure both amplitude and phase screens. However, only the phase screen is required for the DEM calibration - the amplitude screen is used during

radiometric calibration.) The correction function is estimated using a test site with little or no topographic variations, so that residual height errors can be assumed to come from error sources only. All mathematical derivations of a phase screen can be found in [27], In the Integrated Processor, we apply a final phase screen only after all other known error sources have been estimated and removed.

Figure 9 shows an example of an image where the phase screen calibration technique was applied. The image shown is of the Rosamond dry lake in California, which serves as the AIRSAR calibration site, Radar illumination is from the top and the plane was flying from right to left in the image. (The phases in the large black area in the lake could not be unwrapped due to poor signal to noise ratio.) The shades of gray in the image represent elevation (modulated by the radar return for ease of interpretation), with a total relief of 50 meters. The horizontal bands in the image on the left are due to multi-path signals received by the interferometric antennas, It is clear from the image on the left that in this low relief area the height accuracy is limited by the errors introduced by the multi-path signals. The image on the right shows the resulting elevation map after the phase screen due to the multi-path signals was estimated and removed. In addition to showing a dramatic improvement in height accuracy, the height error in the image on the right is no longer dominated by multi-path effects. The resulting r.m.s. height variation in the image on the right, when calculated in small boxes, vary between less than 1.2 meters near the top of the image and 3.5 meters near the bottom of the images (i.e. in the far range) depending on the strength of the backscatter.

VIII. PROCESSOR IMPLEMENTATION

The Integrated Processor is implemented as a collection of stand-alone programs. Which programs are used, and in which order, depends on the AIRSAR/TOPSAR mode that the data were acquired in. First we process all the channels of a particular frequency into multi-looked images in the zero squint geometry. We implemented two versions of the processor to do this. In the first each channel is processed separately and the single-look images are stored on disk, Multi-looking is performed on the various cross-products of the individual channels. The advantage of this approach is that less memory is required for the SAR processor since only one channel is processed at a time, but this advantage is offset by the fact that the large single-look files need to be stored on disk, In the second implementation, we process all channels for each frequency simultaneously, and the cross-product formation and multi-looking are performed in the SAR processor, In this case significantly more memory is used in the SAR processor, but no intermediate single-look files need to be stored.

We utilize the first approach on Hewlett Packard HP 735 workstations to process AIRSAR/TOPSAR images of up to 20 km in the along-track direction (limited by disk size). These workstations have 512 Mbytes of memory, and P-band images are typically

processed to reduced resolution (4.5 m) to fit inside the available memory. The second approach is utilized on a Silicon Graphics Power challenge computer with 2 GBytes of memory to process images up to 80 km long in the along-track direction. As in the case of the HP workstations, P-band data are processed to reduced resolution to fit in the memory. In both cases we use a range-Doppler algorithm as described by Madsen *et al.* [12]. This algorithm was chosen to accommodate a Doppler centroid that varies rapidly as a function of range.

The post processing steps applied after the SAR processing depends on the mode in which the data were acquired. For the three-frequent y polarimetric mode the various cross-products are combined into the standard AIRSAR compressed Stokes Matrix format and then radiometrically calibrated, .

In the case where interferometric data were acquired, the interferogram phase is first unwrapped and the slant range digital elevation model is formed. The location parameters for each slant range pixel is now calculated using the elevation model just derived. Since all the images acquired at the different frequencies now are co-registered, the same set of locations parameters can be used to geometrically resample all images. These location parameters are then used to resample the calibrated polarimetric SAR images. In addition to the calibrated and geometrically corrected SAR images and the digital elevation model, images of the local incidence angle and the interferometric correlation coefficient are also provided. These images are also geometrically corrected using the location parameters previously calculated.

IX. RESULTS AND EXAMPLES

The performance of the TOPSAR instrument and processor was previously reported by Madsen, et *al.* [12], who compared the radar derived digital elevation models with ones derived using conventional optical stereo techniques, Their analysis showed the difference between the DEMs to be 2.2 m r.m.s in relatively flat terrain, and up to 5.0 m in mountainous areas. Instead of repeating these analyses here, we compare the results of the Integrated Processor described here to that of the TOPSAR processor described by Madsen *et al.* [12].

To compare the results of the processors, we processed two strips of data through both processors, and then compared the results. First we tested the relative geometrical accuracy of the two resulting data sets, This is done by cross-correlating small subsections of the images, and measuring the along-track and cross-track offsets between the images. This analysis is repeated for a grid of 100 points spaced uniformly through the images. To test the effect of relief on the results, this comparison was done for a flat area covering the Bolivar peninsula near Galveston, Texas, and a mountainous area covering part of Mount Rainier in Washington State. The digital elevation models for the two areas are

shown in Figure 9. The total relief in the Bolivar scene is less than 50 m while the total relief in the Mount Rainier scene is more than 1500 m The results of the relative geometry test shows the r.m.s. difference between the Bolivar images to be *1.3* m in the cross-track direction, and 2.1 m in the along-track direction for a nominal post spacing of 10 m. For the Mount Rainier scenes, the rms difference are 2.3 m and 4.9 m in the cross- and long-track directions respectively. This confirms previous reports that results for relatively flat areas are typically better than those for high relief areas.

Figure 10 shows an example of multi-frequency and multi-polarization data produced with the Integrated Processor. The area shown in perspective view is in the Cordillera Real region Bolivian Andes near the capital city of La Paz, The three-frequency images are automatically co-registered in the processor, and geometrically resampled using the topography derived from the C-band interferometric data. While a full scientific analysis of the scene is beyond the scope of this paper, the images clearly shows significantly different responses at the different frequencies. All frequencies scatter strongly from the exposed rough rock surfaces near the top of the montains, while the valleys show different variations in grayscale indicating differences in scattering between the different frequencies and polarizations.

X. SUMMARY

In this paper we described the implementation of an integrated SAR processor designed to process data from either polarimetric, interferometric or mixed mode (a combination of polarimetric and interferometric modes) SAR systems. The processor implementation and motion compensation approach, as well as the algorithm used to resample data in the interferometric mode, were described in detail. Calibration of the interferometric and polarimetric data was also discussed in detail. Results from this processor, compared to that produced by an updated verion of the TOPSAR processor previously described by Madsen *et al.* [12] were presented, and these show the results from the two processors to be almost identical. This processor is now used operationally to produce data acquired with the AIRSAR/TOPSAR system for NASA investigators, and it is anticipated that the simultaneous use of digital topographic information and multi-frequency polarimetric SAR data will significantly improve our scientific understanding of scattering from different types of Earth terrain.

REFERENCES

[1] J. J. van Zyl., H.A. Zebker and C. Elachi, "Imaging radar polarization signatures: Theory and observations," *Radio Science, 22,* pp. 529--543, 1987.

[2] H. A. Zebker, J. J. van Zyl and D.N. Held, "Imaging radar polarimetry from wave synthesis," *Journal of Geophysical Research,* 92, no. B1, pp. 683--701, 1987.

[3] J. J. van Zyl, "SAR polarimetry and interferometry," in *Review of Radio Science 1993-1996,* R.W. Stone (Ed), Oxford University Press, New York, 1996.

[4] L. C. Graham, "Synthetic Interferometer Radar for Topographic Mapping," *Proc. IEEE, 62,* pp.763-768, *1974.*

[5] H. Zebker and R. Goldstein, "Topographic Mapping from Interferometric SAR Observations," *J. Goephys. Res.,* **91,** pp. 4993-4999, 1986.

[6] C. T Allen, "Interferometric Synthetic Aperture Radar," *IEEE Geoscience and Remote Sensing Society Newsletter,* pp. 6-13, September 1995.

[7] R. M. Goldstein, H. A. Zebker, and C. Werner, "Satellite Radar Interferometry: Two-Dimensional Phase Unwrapping," *Radio Sci.,* 23, pp. 713-720, 1988.

[8] F.K. Li, and R. M. Goldstein, "Studies of Multibaseline Spaceborne Interferometric Synthetic Aperture Radars," *IEEE Trans. Geosci. Remote Sens.,* **GRS-28,** pp. 88-97, 1991.

[9] J.C. Curlander and R. N. McDonough, *Synthetic Aperture Radar Sytems and Signal Processing,* John Wiley and Sons, New York, 1991.

[10] H. A. Zebker, S. N. Madsen, J. Martin, K. B. Wheeler, T. Miller, Y. Lou, G. Alberti, S. Vetrella, and A. Cucci, "The TOPSAR interferometric Radar Topographic Mapping Instrument," *IEEE Trans. Geosci. Remote Sens., GRS-30,* pp. 933-940, 1992,

[11] N. P. Failer and E, H. Meier, "First results with the airborne single-pass DO-SAR interferometer," *IEEE Trans. Geosci. Remote Sens.,* **GRS-33,** pp. 1230-1236, 1995.

[12] S. N. Madsen, H. A. Zebker, and J. Martin, "Topographic Mapping Using Radar Intereferometry: Processing Techniques," ," *IEEE Trans. Geosci. Remote Sens.,* **GRS-31,** pp. 246-256,1993.

[13] D. L. Evans (Ed.) *Spaceborne Synthetic Aperture Radar: Current Status and Future Directions,* Nasa Technical Memorandum 4679, NASA Scientific and Technical Office, 1995.

[14] Y. Lou, Y Kim and J.J. van Zyl, "The NASA/JPL Airborne Synthetic Aperture Radar System," *Summaries of the Sixth Annual Airborne Science Workshop, Volume II: AIRSAR Workshop,* Held March 4-8, 1996 at JPL, Pasadena, CA, pp. 51-55, 1996.

[15] Stofan, E. R., D.L. Evans, C. Schmullius, B. Holt, J.J. Plaut, J. van Zyl and J. Way, "Overview of results of Spaceborne Imaging Radar-C, X-Band Synthetic Aperture Radar (SIR-C/X-SAR)," *IEEE Transactions on Geoscience and Remote Sensing, GE-33,* pp. 817-828,1995.

[16] R.M. Goldstein, and H. A. Zebker, "Interferometric Radar Measurements of Ocean Surface Currents," *Nature, 328,* pp. 707-709, 1987.

[17] R. E. Carande, "Estimating Ocean Coherence Time Using Dual-Baseline Interferometric Synthetic Aperture Radar," *IEEE Trans. Geosci. Remote Sens., GRS-32,* pp. 846-854,1994.

[18] J.J van Zyl., H.A. Zebker, S. Hensley and D.R. Haub, "The new dual frequency (C- and L-band) TOPSAR airborne interferometric SAR," *Proceedings of IGARSS'95*, Florence, Italy, July 10-14, pp. 1995.

[19] Y. Lou and J.J. van Zyl, "Relative phase calibration of the NASA/DC-8 three-frequency polarimetric SAR system," *Proceedings of IGARSS'92,* Houston, Texas, May 26-29, pp. 104-105,1992.

[20] J.J. van Zyl, "A Technique to Calibrate Polarimetric Radar Images Using Only Image Parameters and Trihedral Corner Reflectors," *IEEE Trans. Geosci. Remote Sens., GRS-28, pp. 337-348,1990.*

[21] A.L. Gray, P.W. Vachon, C.E. Livingstone, and T.I. Lukowski, "Synthetic Aperture Radar Calibration using Reference Reflectors," *IEEE Trans. Geosci. Remote Sens., GRS-28, pp. 374-383,1990.*

[22] J.J. van Zyl, B. Chapman, P. Dubois, and J.C. Shi, "The effect of topography on SAR calibration," *IEEE Transactions on Geoscience and Remote Sensing, GE-31,* pp. 1036-1043, 1993.

[23] F.T. Ulaby and C. Elachi (Ed.), *Polarimetry for Geoscience Applications,* Chapter 6, Artech House, Inc., 1990.

[24] H.J. Kramer, *Observation of the Earth and Its Environment: Survey of Missions and Sensors, 3* rd Edition, Springer Verlag, New York, NY, 1996.

[25] Department of Defense World Geodetic System 1984 - Its definition and relationships with other local geodetic systems, DMA Techical Report 8350.2, Defense Mapping Agency, Washigton, D. C., 1987.

[26] S. Hensley and S.N. Madsen, "A convenient coordinate system for Radar remote sensing applications," ," To be Submitted to *IEEE Transactions on Geoscience and Remote Sensing, 1997.*

[27] Y. Kim, S. Hensley, D. Imel, and E. Chapin, "Interferometric SAR calibration," To be Submitted to *IEEE Transactions on Geoscience and Remote Sensing, 1997.*

Tables

Table 1. Summary of the available radar modes for AIRSAR. ***** Since 1994, P-band is allowed to transmit in the US only when the radar is in 20 MHz chirp bandwidth mode. If special clearance is obtained prior to the flight, P-band is then allowed to transmit in 40 MHz chirp bandwidth mode also.

Mode	Date	P-band*		L-band		C-band	
		TX	RX	TX	RX	TX	RX
POLSAR (quad-pol)	1988- present	P-SAR (H/V)		L-SAR (H/V)		C-SAR (H/V)	
ATI	1988-1990	P-SAR (H/V)		L-fwd and L-SAR		C-fwd and C-SAI	
ATI	1991- present	P-SAR (H/V)		L-fwd and L-SAR		C-bt (V) and C-SA	
XTI1	1991	P-SAR (H/V)		L-SAR (H/V)		C-bt	C-bt / C-t
XTI1	1992-1995	P-SAR (H/V)		L-SAR (H/V)		C-tp	C-bt / C-t
XTI1 - ping pong	1995	P-SAR (H/V)		L-SAR (H/V)		C-bt and C-tp	
XT12	1995	P-SAR (H/V)		L-tp	L-tp / L-bt	C-tp	C-bt / C-t
XT12 - ping pong	1995	P-SAR (H/V)		L-tp and L-bt		C-bt and C-tp	

Figure Captions

Figure 1. Geometry assumed in traditional non-interferometric SAR processing. The scatterer is assumed to be at the intersection of the range sphere, the Doppler cone, and an assumed flat reference plane. The case shown is for a left looking SAR.

Figure 2. In the case of interferometric SAR processing, one does not have to assume all scatterers are on a flat reference plane. Instead, the scatterer is at the intersection of the range sphere, the Doppler cone, and the interferometric phase cone. Thus, the additional information contained in the interferometric phase allows one to automatically generate images and digital elevation maps that are geometrically corrected for the imaging geometry.

Figure 3. Coordinate systems used to describe geometry in the Integrated Processor. The images are defined in a "global" coordinate system denoted by (s, c, h), where $\hat{\mathbf{s}}$ is a unit vector pointing in the positive along-track direction, $\hat{\mathbf{c}}$ is a unit vector pointing in the positive cross-track direction (to the left of $\hat{\mathbf{s}}$) and $\hat{\mathbf{h}}$ points up. The instantaneous imaging geometry is described by a a "local" coordinate system denoted by (x, y, z) In the absence of aircraft yaw, pitch and roll, the two coordinate systems are the same,

Figure 4. The motion compensation scheme used in the Integrated, Processor, All images are reference to a *common* global reference line. However, when processing data, individual images are first compensated to a local reference line. After image formation individual images are referenced to the common global line. The antenna paths assumed during processing are the averages of the transmit and receive antenna paths. The case shown in this figure is for a single baseline operation, with the upper antenna transmitting and receiving, while the bottom antenna is only receiving.

Figure 5. Geometry showing the corrections needed to transform from coordinates of a point from the Cartesian coordinate system to that on a three-dimensional spherical surface.

Figure 6. Right triangle used to calculate the correction to the elevation of a point when going from the Cartesian coordinate system to a three-dimensional spherical surface approximation.

Figure 7. Right spherical triangle used to calculate spherical corrections to the along-track and cross-track positions of a pixel.

Figure 8. Images of Tennesy Valley in Northern California showing the effects of taking the topography into account when performing radiometric corrections. The image covers part of Marin County north of San Francisco. The image on the left was calibrated taking

the topography inot account, while the image on the right was calibrated assuming a flat earth, as is done in most traditional SAR processors. Note most of the brightness modulation in the image on the right is no longer present in the image on the left. This means that most of the difference in brightness between the slopes facing the radar and those facing away from it is in fact due to the uncompensated scattering areas, and not really due to the influence of the incidence angle on the scattering from the terrain.

Figure 9. The image shown is of the Rosamond dry lake in California, which serves as the AIRSAR calibration site, Radar illumination is from the top and the plane was flying from right to left in the image. The phases in the large black area in the lake could not be unwrapped due to poor signal to noise ratio. The shades of gray in the image represent elevation, modulated by the radar returns for ease of interpretation. The horizontal bands in the image on the left are due to multi-path signals received by the interferometric antennas.

Figure 10. Perspective views of part of the Bolivian Andes near La Paz, **Bolivia.** The topography was derived from C-band TOPSAR interferometric data. Draped over the topography are the grayscale radar images acquired at L-band HH, C-band VV, and P-band HH. The aircraft was flying from right to left above and behind this view, so that the part of the scene closest to the observer was actually in the far range of the original radar image. The many variations in color indicate difference in scattering properties as measured by the difference frequencies and polarizations.

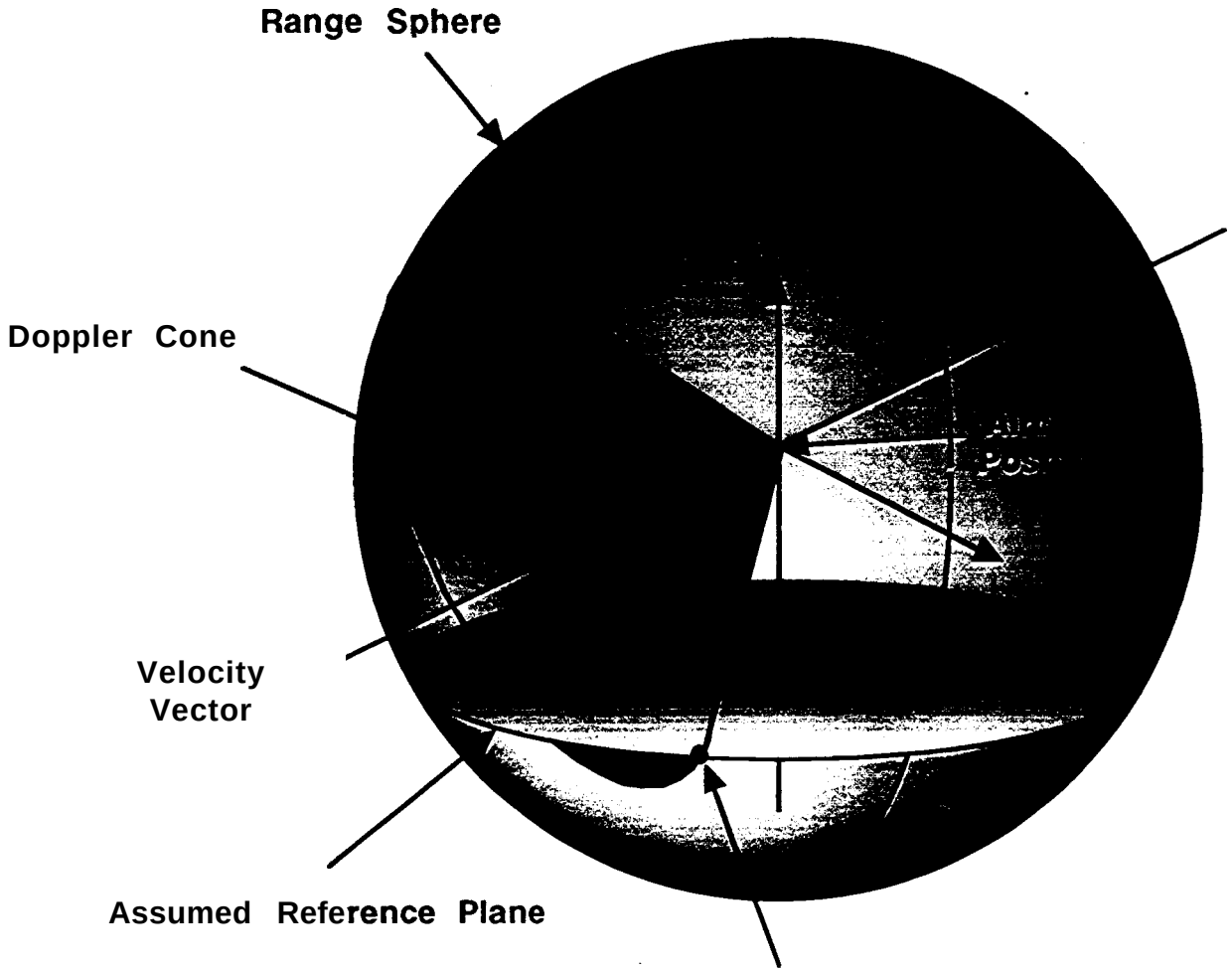

Figure 1. van Zyl *et al.*

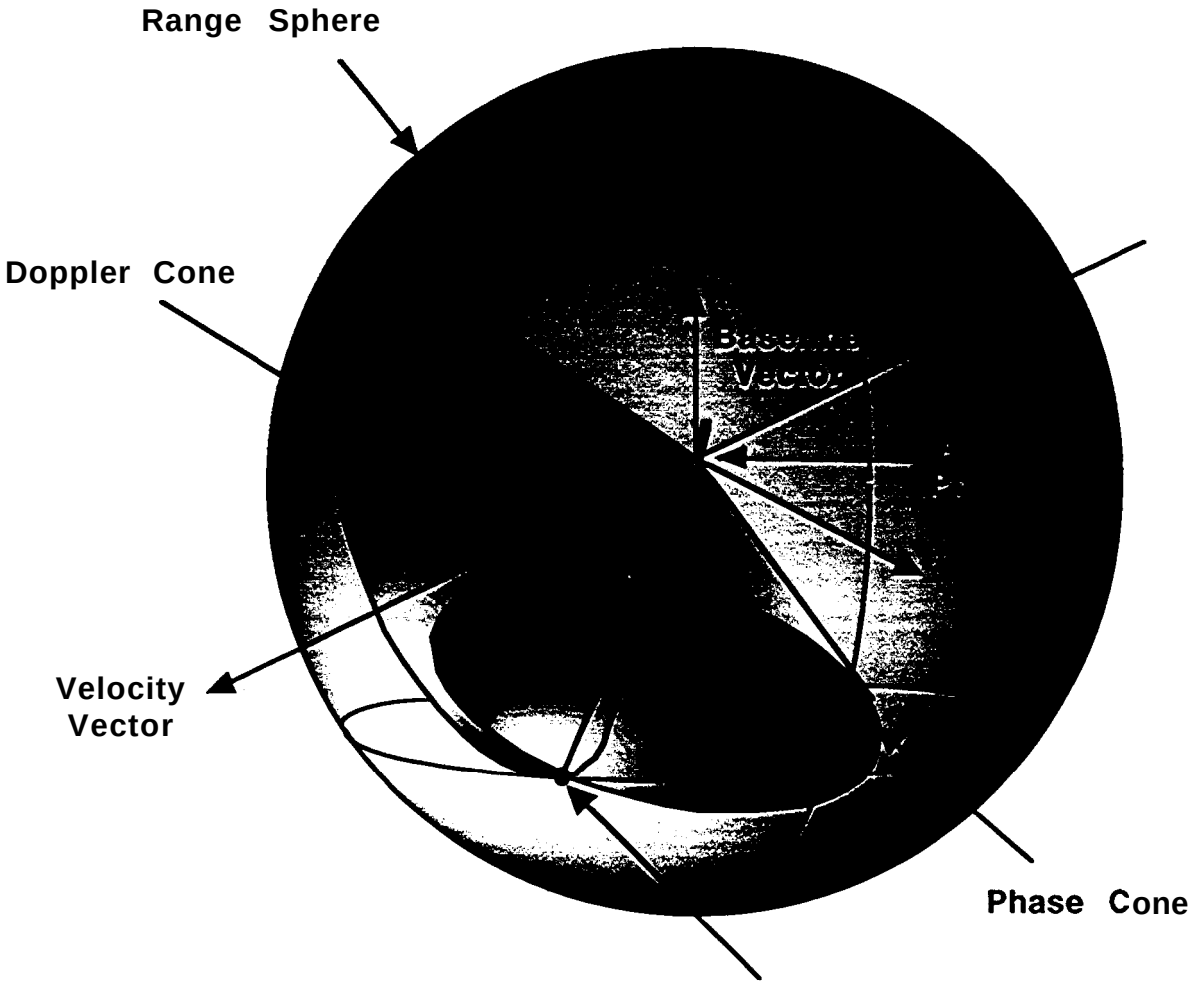

Figure 2. van Zyl *et al.*

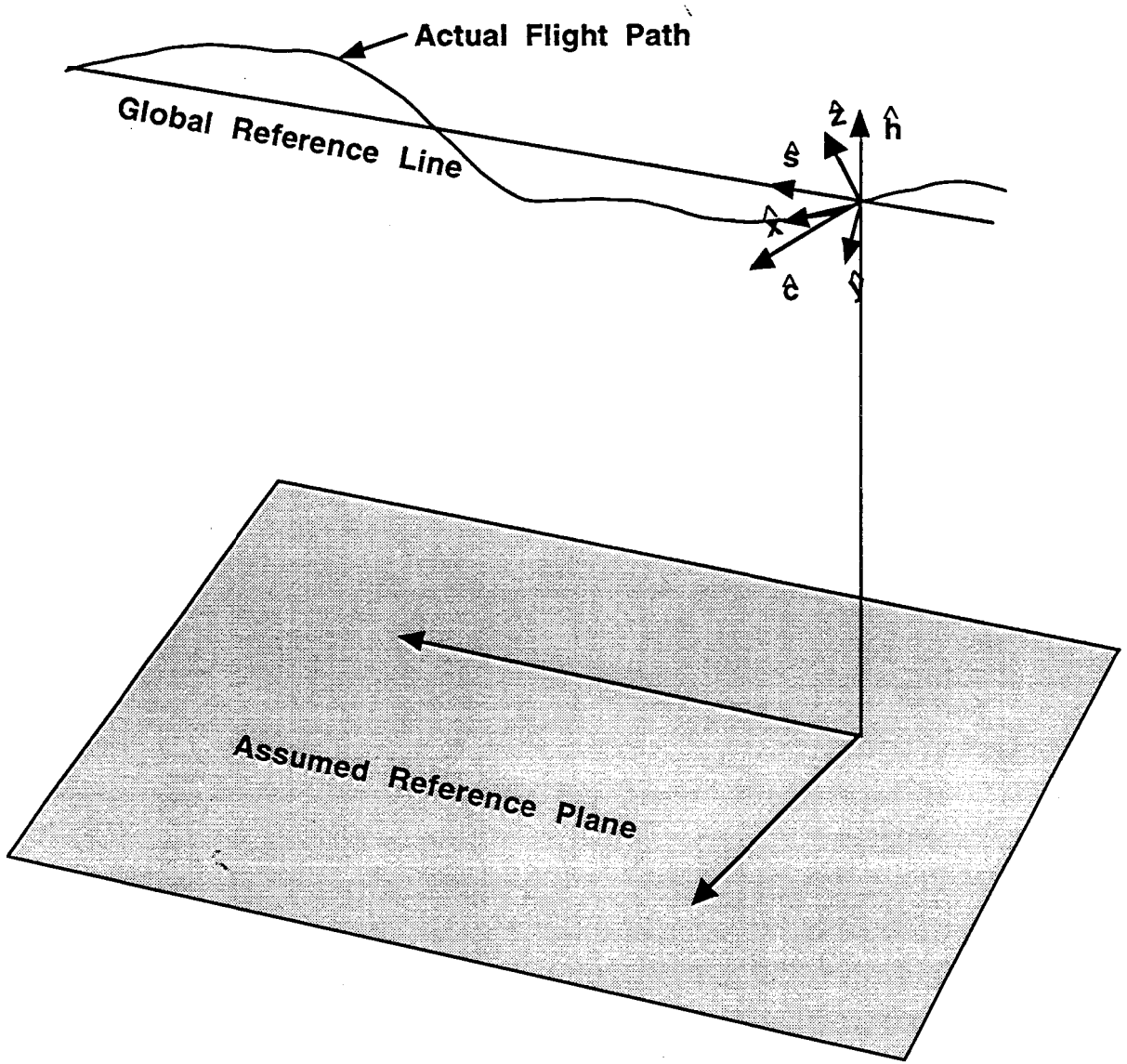

Figure 3. van Zyl *et al.*

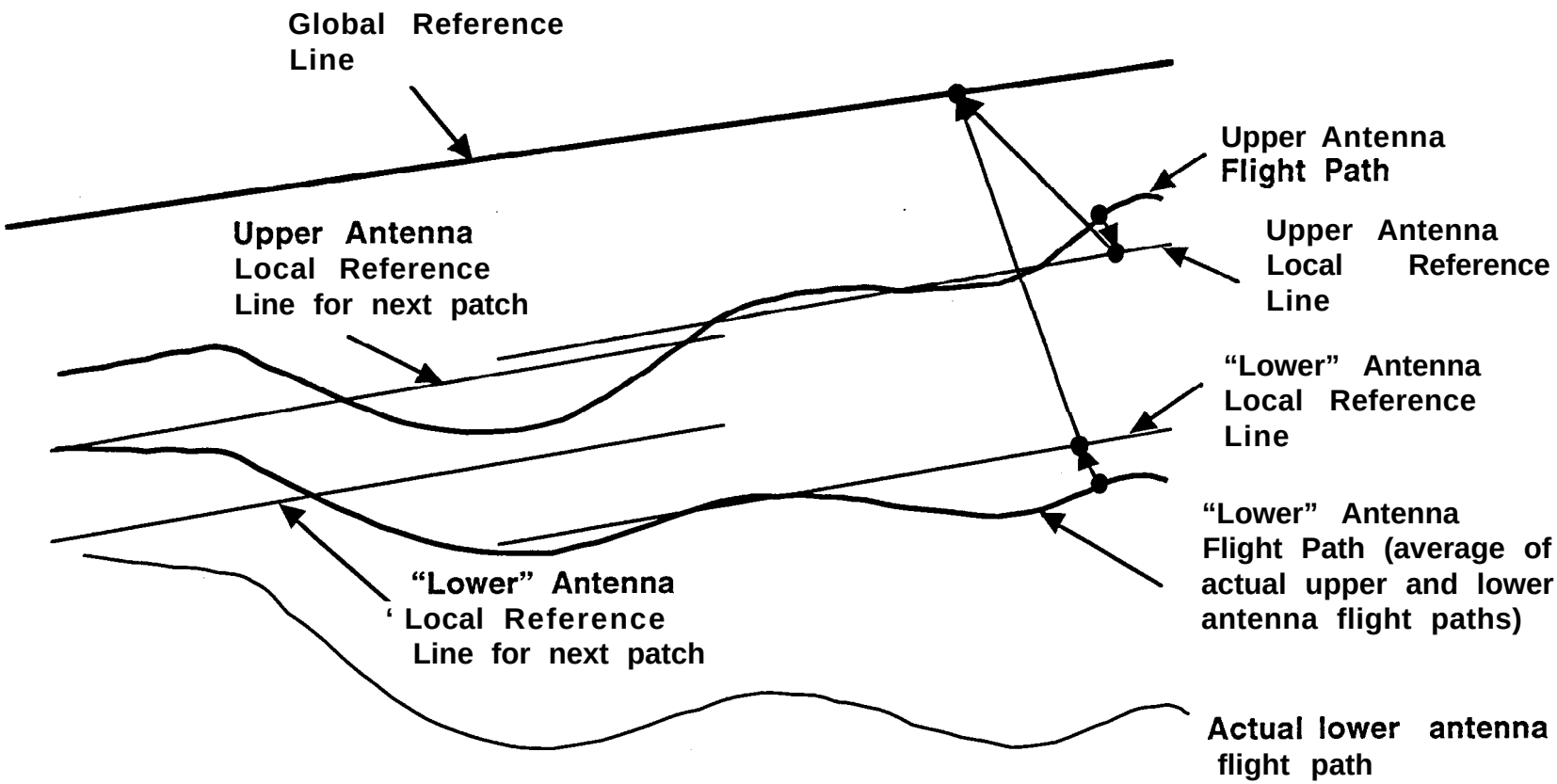

Figure 4. van Zyl *et al.*

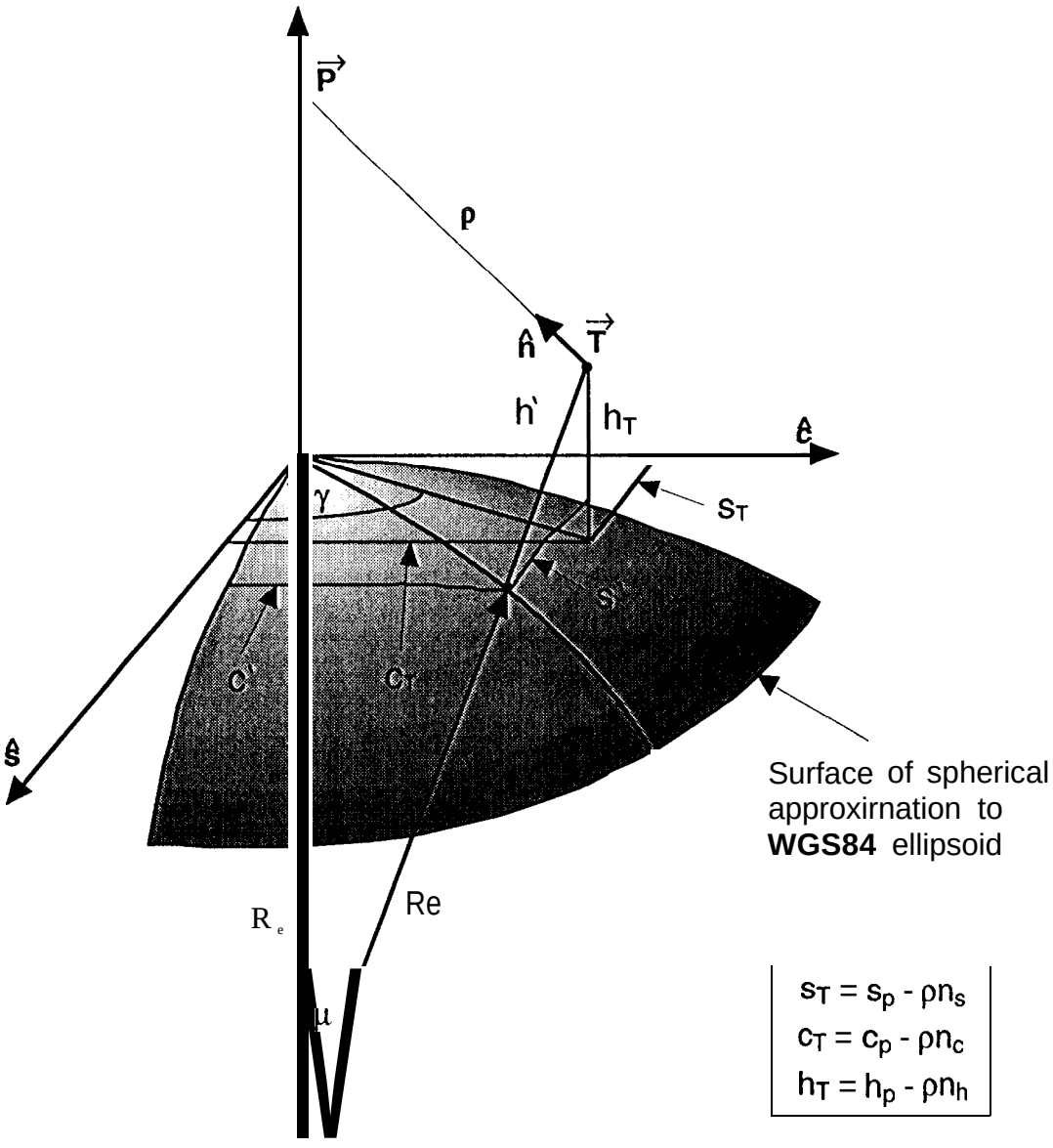

Figure 5. van **Zyl eta/.**

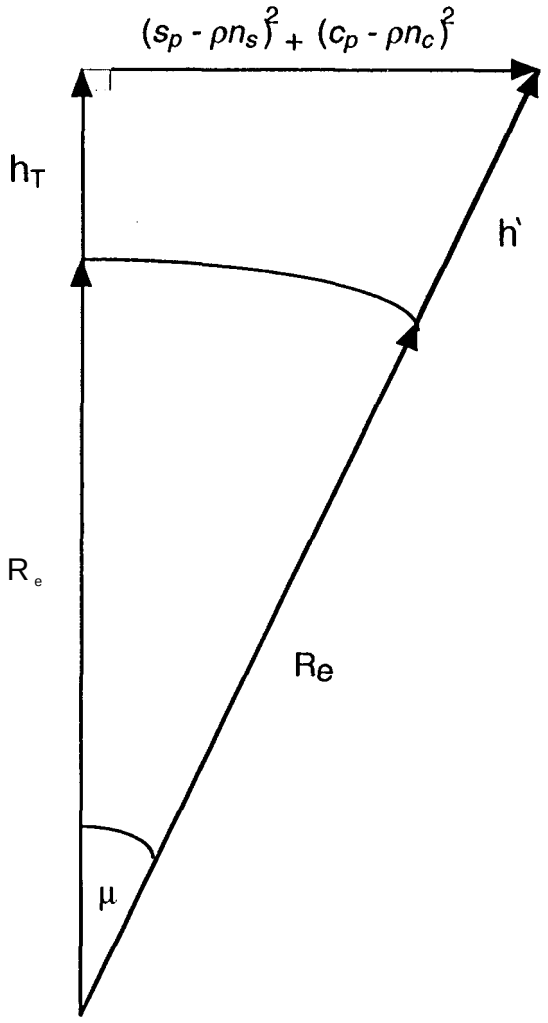

Figure 6. van *Zyl eta/.*

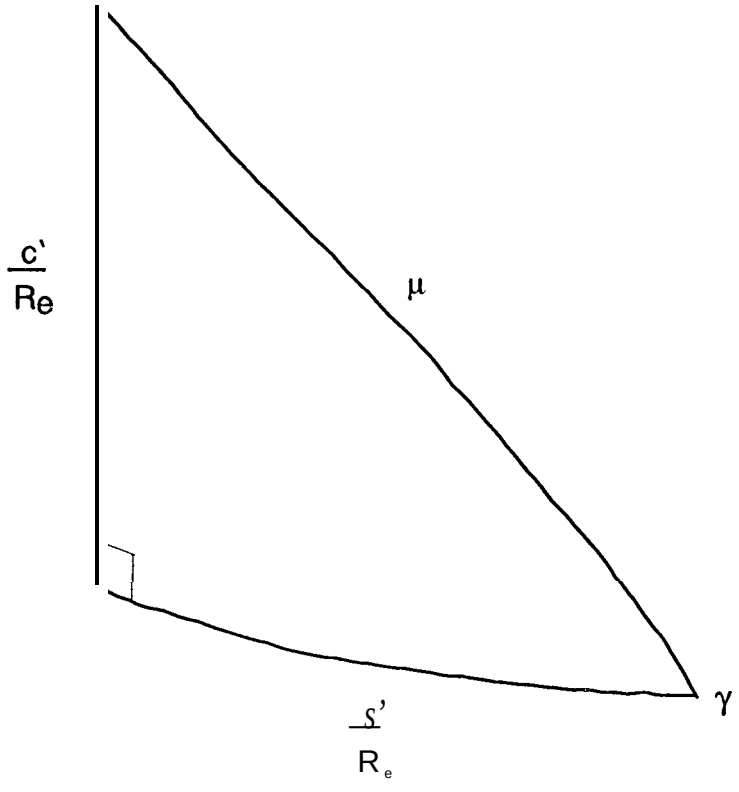

Figure 7. van Zyl *et al.*

TENNESSEE VALLEY, CALIFORNIA

C-BAND VV

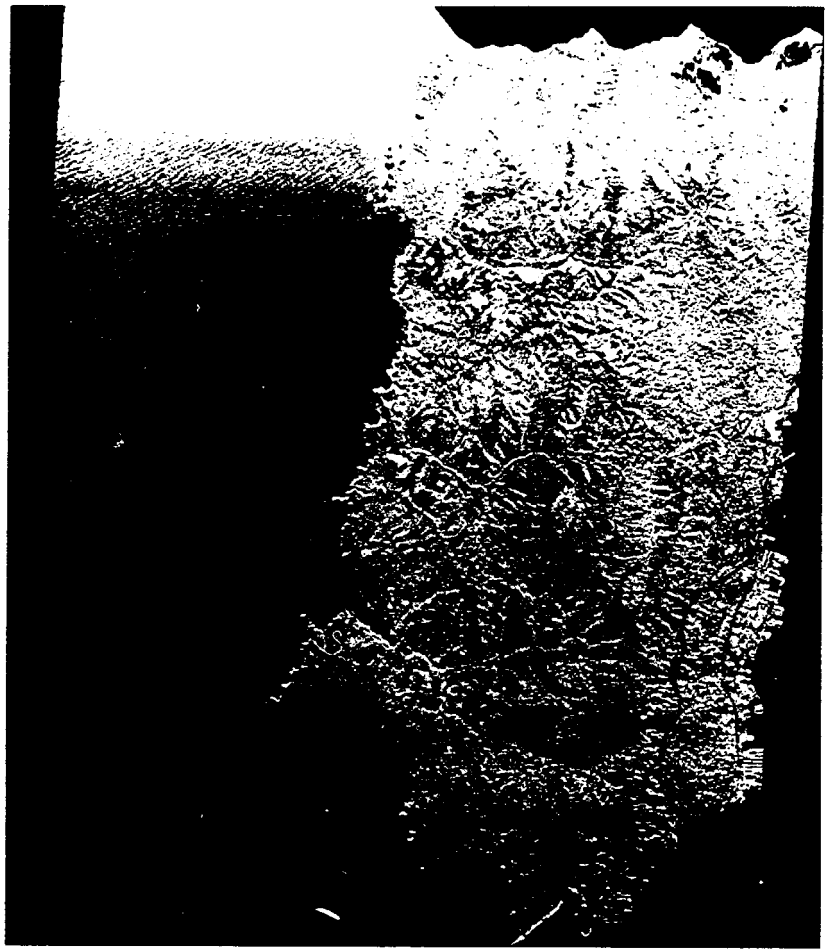

CALIBRATED TAKING TOPOGRAPHY INTO ACCOUNT

CALIBRATED ASSUMING A FLAT EARTH

Figure 8. van Zyl et al.

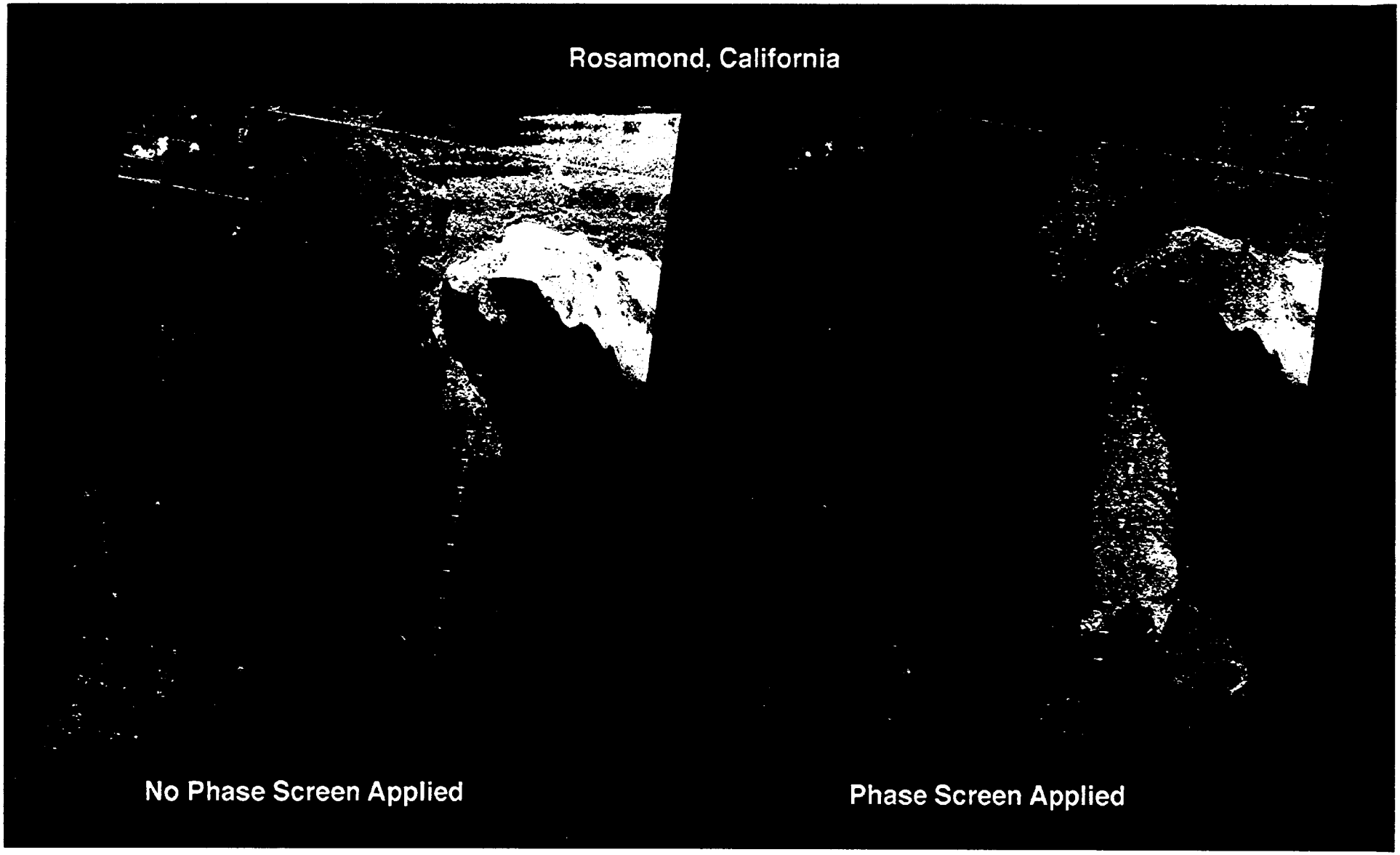

Figure 9. van Zy et al.

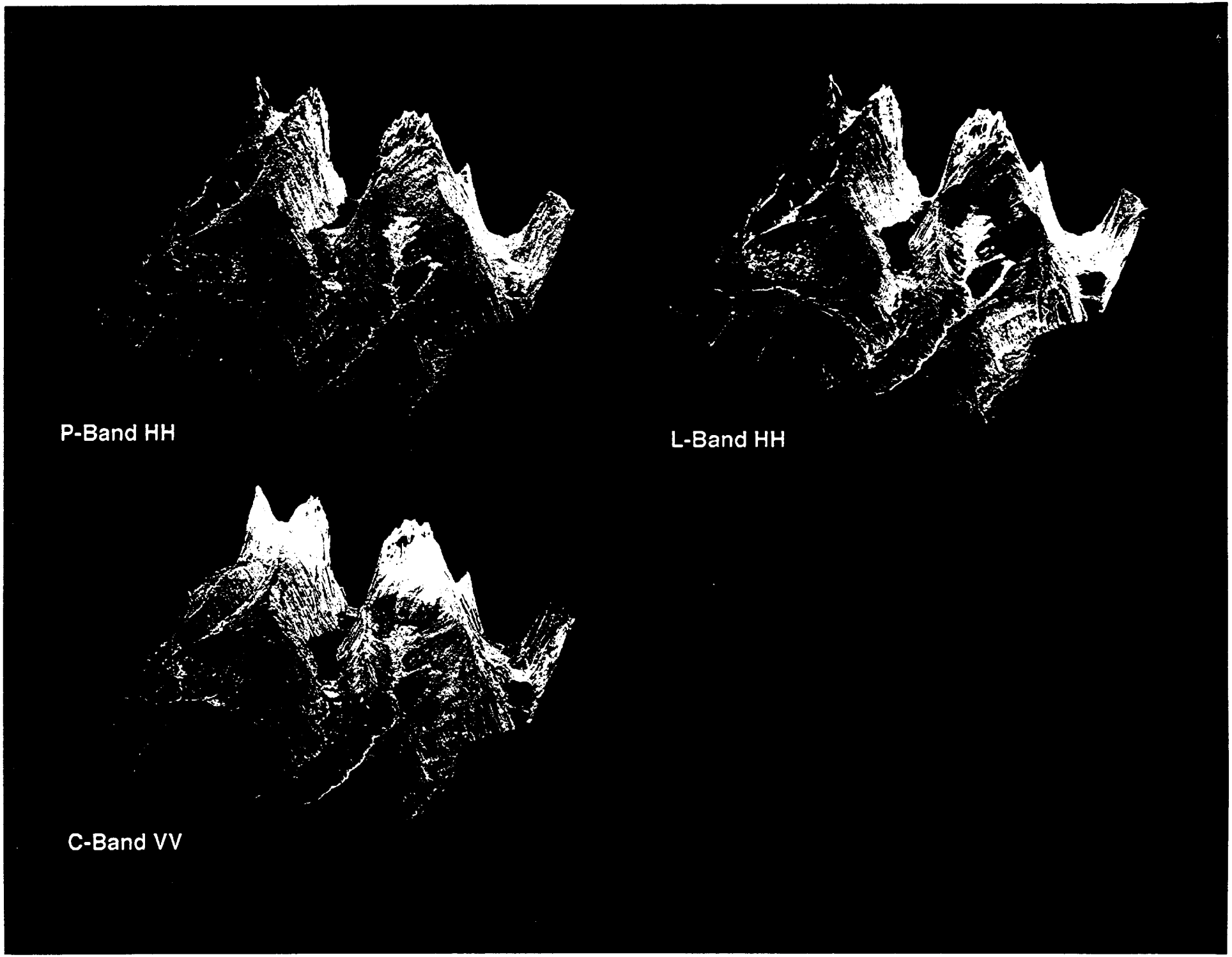

Figure 10. van Zyl et al.